Research Article

Shabbir Ahmed Khan, Fahim Ahmed*, Najam Ul Hassan, Muhammad Zulfiqar, Muhammad Nauman Usmani, Asma A. Alothman, Saikh Mohammad, Md Rezaul Karim*, and Dongwhi Choi*

Tuning structural and electrical properties of Co-precipitated and Cu-incorporated nickel ferrite for energy applications

https://doi.org/10.1515/ntrev-2024-0017
received February 1, 2024; accepted March 25, 2024

Abstract: The $Ni_{1-x}Cu_xFe_2O_4$ (where x = 0, 0.05, 0.10, 0.15) nano ferrite powder was synthesized through chemical co-precipitation method, NaOH and acid oleic as raw materials. The XRD patterns confirmed the spinal structure phase purity of materials. XRD results showed that lattice parameter decreases with the increase of copper concentration by increasing copper concentration in the parent material. Scanning electron microscopy (SEM) was used to determine the morphology and particle size. SEM analysis indicated that all the samples are in nano size and homogeneous. AC electrical properties of nanoparticles were investigated by employing impedance spectroscopy. The real and the imaginary parts of impedance, permittivity, modulus along with the real part of ac conductivity, and tan delta were measured and analyzed for all synthesized samples in 1 Hz to 7 MHz for different voltages at 300 K.

Keywords: Cu doped nickel ferrite ($Ni_{1-x}Cu_xFe_2O_4$), XRD, SEM, impedance spectroscopy

*** Corresponding author: Fahim Ahmed,** Department of Physics, Division of Science and Technology, University of Education, Lahore 54000, Pakistan, e-mail: Fahim.ahmed@ue.edu.pk
*** Corresponding author: Md Rezaul Karim,** School of Chemical Engineering, Yeungnam University, 280 Daehak-ro, Gyeongsan, Gyeongbuk, 38541, Republic of Korea, e-mail: rezaul@yu.ac.kr
*** Corresponding author: Dongwhi Choi,** Department of Mechanical Engineering (Integrated Engineering Program), Kyung Hee University, 1732 Deogyeong-daero, Yongin, Gyeonggi, 17104, Republic of Korea, e-mail: dongwhi.choi@khu.ac.kr
Shabbir Ahmed Khan: Department of Physics, The University of Lahore, Sub-campus Sargodha, Sargodha, Pakistan
Najam Ul Hassan: Department of Physics, Division of Science and Technology, University of Education, Lahore 54000, Pakistan
Muhammad Zulfiqar: Department of Physics, University of Sargodha, 40100, Sargodha, Pakistan
Muhammad Nauman Usmani: Institute of Physics, Bahauddin Zakariya University, Multan, Pakistan
Asma A. Alothman, Saikh Mohammad: Department of Chemistry, College of Science, King Saud University, Riyadh, 11451, Saudi Arabia

1 Introduction

Ferrites are used in a variety of applications as they exhibit remarkable magnetic and electrical properties [1–3]. Spinel ferrites play an integral role in devices such as high-density information storage devices and in magnetic resonance imaging techniques [4–6]. Nickel ferrite is considered an important soft ferrite material among other materials because of its distinctive characteristics [7–9]. These include nominal losses in eddy current and lower values of electrical conductivity, and they also possess higher chemical stability [10–12]. Nickel ferrite ($NiFe_2O_4$) exhibits counter spinal structure. It is utilized in a variety of technical applications, *i.e.* gas sensors, for the purification of water and also as catalyst [13–15]. It is observed that nickel ferrite ($NiFe_2O_4$) properties are highly dependent on the variation of the composition and also on the route it has been synthesized. Literature shows various methods including the Sol-Gel technique, hydrothermal synthesis, solid-state reaction method, and co-precipitation method are used commonly for its preparation [16–18]. Co-precipitation method is regarded as the simplest, and the low temperature required for sintering and cost-effective technique among others. In this research, we have also used Co-precipitation for the synthesis of our samples [19–21]. In addition to the quick production of a uniform end product, this approach should also allow for the efficient separation of precipitates from the liquid solution and the ability to control or modify the size of the particles [22–24]. The key factor in the co-precipitation process is the careful selection of solvent, with water commonly being employed as the solvent [25–27]. Nevertheless, organic solvents can be employed, but at a significant expense [28–30]. Temperature is a fundamental component that is crucial in regulating

particle size and the creation of different phases [31,32]. The co-precipitation process occurs at the ambient temperature, often within the range of 323–373 K, in order to expedite the precipitation. The pH value of the medium is the primary determinant in co-precipitation, as it strongly influences the phase formation. To achieve favorable results, it is recommended to maintain a pH level of approximately 12 [33–35].

In the literature, various reports show the study of $NiFe_2O_4$ in various compositions. Zheng *et al.* reported $NiFe_2O_4$-FeNi/C (NFO-FN/C) composites by confinement pyrolysis of the polydopamine for large-scale preparation and for the enhanced EMW absorption [36–38] Another report shows the synthesis of $NiFe_2O_4$ NPs and explored the uses in biomedical applications [39]. Gouadria *et al.* reported $LaFeO_3/NiFe_2O_4$ nanohybrid for their efficient use in the photodegradation process [40]. Singh *et al.* studied the mixing of $NiFe_2O_4$ with Cu-doped ZnO (ZnO-Cu) for antibacterial applications [41]. Similarly, various other reports show the study of $NiFe_2O_4$ in various forms of compositions and composites and their potential applications referring towards the importance and large-scale production for soft ferrites [42–47]. This work intends to enhance the understanding further of how the addition of copper affects several properties of nickel ferrites, building upon existing literature on the subject.

This research study employs many methodologies to analyze the structure and electrical properties of the $Ni_{1-x}Cu_xFe_2O_4$ (where x = 0, 0.05, 0.10, 0.15) system. Due to the difference in the copper and nickel ionic radius, Cu caused lattice distortion and changes in the crystal structure when substituted. Copper doping can alter the electrical conductivity and polarization mechanisms in ferrite, enhancing dielectric parameters including permittivity and loss tangent. The synthesis of nano ferrite powder was achieved through chemical co-precipitation using NaOH and acid oleic. X-ray diffraction (XRD) was employed to analyze the structural properties of the powder. The XRD patterns revealed the high purity of synthesized samples. According to XRD analysis, the lattice parameter decreases as the copper level in the parent material increases. The

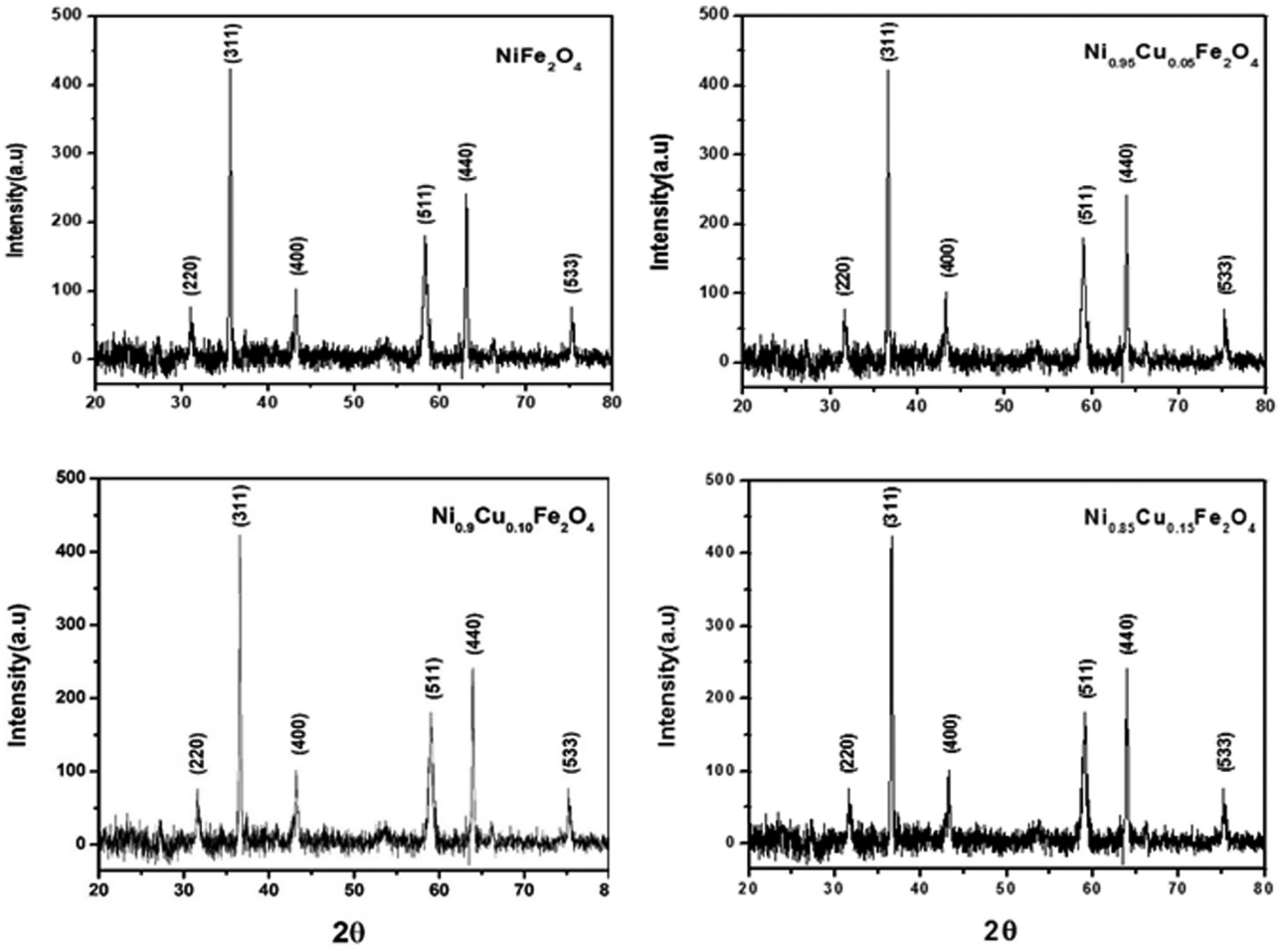

Figure 1: Powder XRD patterns of $Ni_{1-x}Cu_xFe_2O_4$ (where x = 0, 0.05, 0.10, 0.15).

particle size and shape were assessed using scanning electron microscopy (SEM). The scanning electron microscopy (SEM) analysis revealed that all samples exhibited a uniform and nanoscale size distribution. Alternating current impedance spectroscopy was employed to investigate the electrical properties of nanoparticles. The impedance, permittivity, modulus, AC conductivity, and tan delta of all compositions were analyzed at room temperature for different voltages over a frequency range of 1 Hz to 7 MHz.

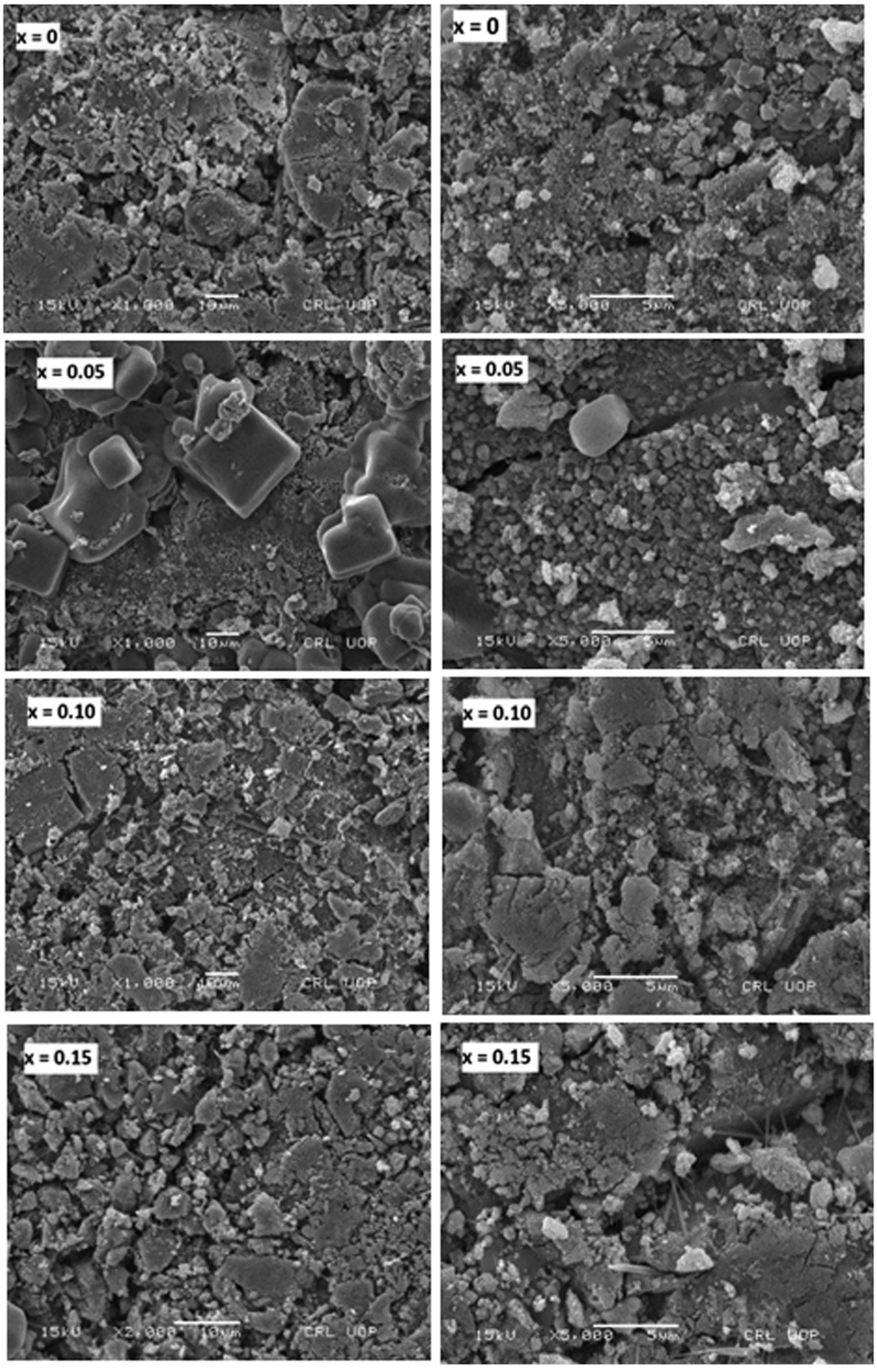

Figure 2: SEM images of $NiFe_2O_4$, $Ni_{0.95}Cu_{0.05}Fe_2O_4$, $_{0.90}Cu_{0.10}Fe_2O_4$, and $Ni_{0.85}Cu_{0.15}Fe_2O_4$ nanoparticles.

2 Experimental method

Nickel ferrite ($NiFe_2O_4$) samples were prepared by employing the co-precipitation method. Using sodium hydroxide (NaOH) 3 molar solutions, the precipitating agent is prepared. 0.4 Molar ferric chloride ($FeCl_3{\cdot}6H_2O$ > 99%) and 0.2 molar nickel chloride ($NiCl_2{\cdot}6H_2O$ > 99%) and $CuCl_2{\cdot}2H_2O$ > 99% solution was made and mixed slowly with the precipitating agent. NaOH solution was added dropwise while keeping note of pH. The reactants are continuously stirred with the help of a magnetic stirrer until a pH level of greater than 12 is achieved. As surfactant, oleic acid (2–3 drops) is mixed with the solution. Subsequently, this precipitate is stirred for about 40 min while maintaining the temperature to 80°C. The material being treated is then allowed to cool to room temperature. After that in order to expel the undesirable impurities and surfactant the sample under preparation is washed two times by ethanol and distilled water. In the centrifuge machine, the sample is centrifuged at a rate of 2,000 revolutions per minute (rpm), for about 15 min. It is then followed by an overnight drying session in an oven where the material is dried at 80°C. The material taken from the oven is then ground well to make it into powder form. Finally, it was subjected to a high temperature of 600°C in a furnace for 10 h. After the synthesis of the parent material, the next process is to fabricate the pellets before the execution of characterization. For the fabrication of the circular-shaped pellets hydraulic press is utilized. It exerted a pressure of 6 tons/inch^2 for the duration of 2 min. The diameters of these pellets are 10 mm, and the thickness is maintained to 1.5 mm. After their fabrication, the pellets are subjected to the sintering process in a furnace. In the furnace, the temperature is kept at 600°C for 10 h. The final product after sintering is ready for further characterization processes. SEM instrument the structural properties of the synthesized powders are studied. The JSM5910 model of SEM is used for imaging the prepared samples, which is manufactured by JEOL, Japan. For impedance spectroscopy, the Alpha-N Analyzer, Novo control, Germany, was used that is installed in PINSTECH, Islamabad

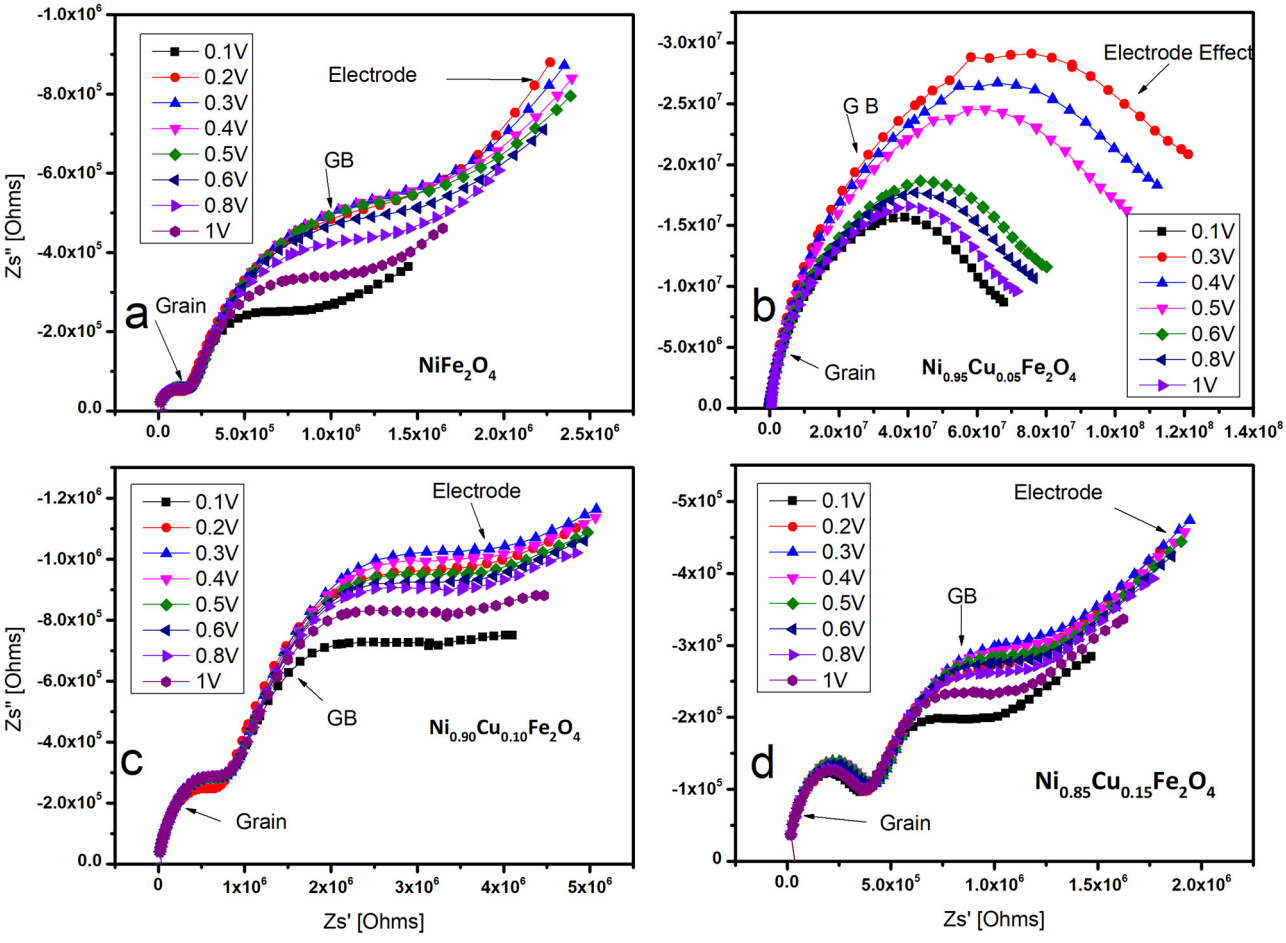

Figure 3: Complex impedance plots of (a) $NiFe_2O_4$, (b) $Ni_{0.95}Cu_{0.05}Fe_2O_4$, (c) $Ni_{0.90}Cu_{0.10}Fe_2O_4$, and (d) $Ni_{0.85}Cu_{0.15}Fe_2O_4$ from 0.1 to 1 V.

3 Results and discussion

3.1 XRD analysis

XRD Pattern for the parent sample ($NiFe_2O_4$) is shown in Figure 1(a). The diffraction pattern of the sample is analyzed, and the formation of spinal cubic structure is confirmed. The average crystallite size of the parent sample has been calculated from the full-width at half-maximum (FWHM) using the Scherrer formula [48]

$$D = \frac{0.9\lambda}{\beta \cos\theta}, \tag{1}$$

where D is the crystallite size, λ is the wavelength of the X-ray, β is full width at half maximum (FWHM) measured in radians, and θ is the Bragg angle. The X-ray diffraction pattern of the parent sample heated at 600°C is prepared by employing the co-precipitation method, all of the peaks shown in the pattern were successfully indexed. XRD result shows a single-phase cubic spinel structure with an average crystallite size of 40.52 nm. X'Pert Pro, Analytical, Netherlands machine is used for X-ray diffraction. By utilizing Cu Kα radiation (1.5418 Å) in XRD, the phase purity of the sintered pellets was affirmed. With a scanning step and counting time of 0.02° and 3 s, respectively, the XRD data were taken for 20° ≤ 2θ ≤ 80° by maintaining the temperature to room temperature. XRD pattern collected at room temperature of freshly synthesized parent sample ($NiFe_2O_4$). All of the peaks shown in the pattern were successfully indexed.

The lattice parameter here determined from XRD data is a = 8.3400 Å. The lattice constants are reduced by increasing copper doping in the studied composition shown in Figure 1(b)–(d). This could be referred to the difference in the ionic radius of Cu ions being smaller ionic radius (0.73 Å) than Ni (0.74 Å) and Fe ions (0.67 Å) [49,50]. The cell volume of the parent sample is 580.09 $Å^3$, and it is greater than the doped samples. The main diffraction planes are (220), (311), (400), (511),

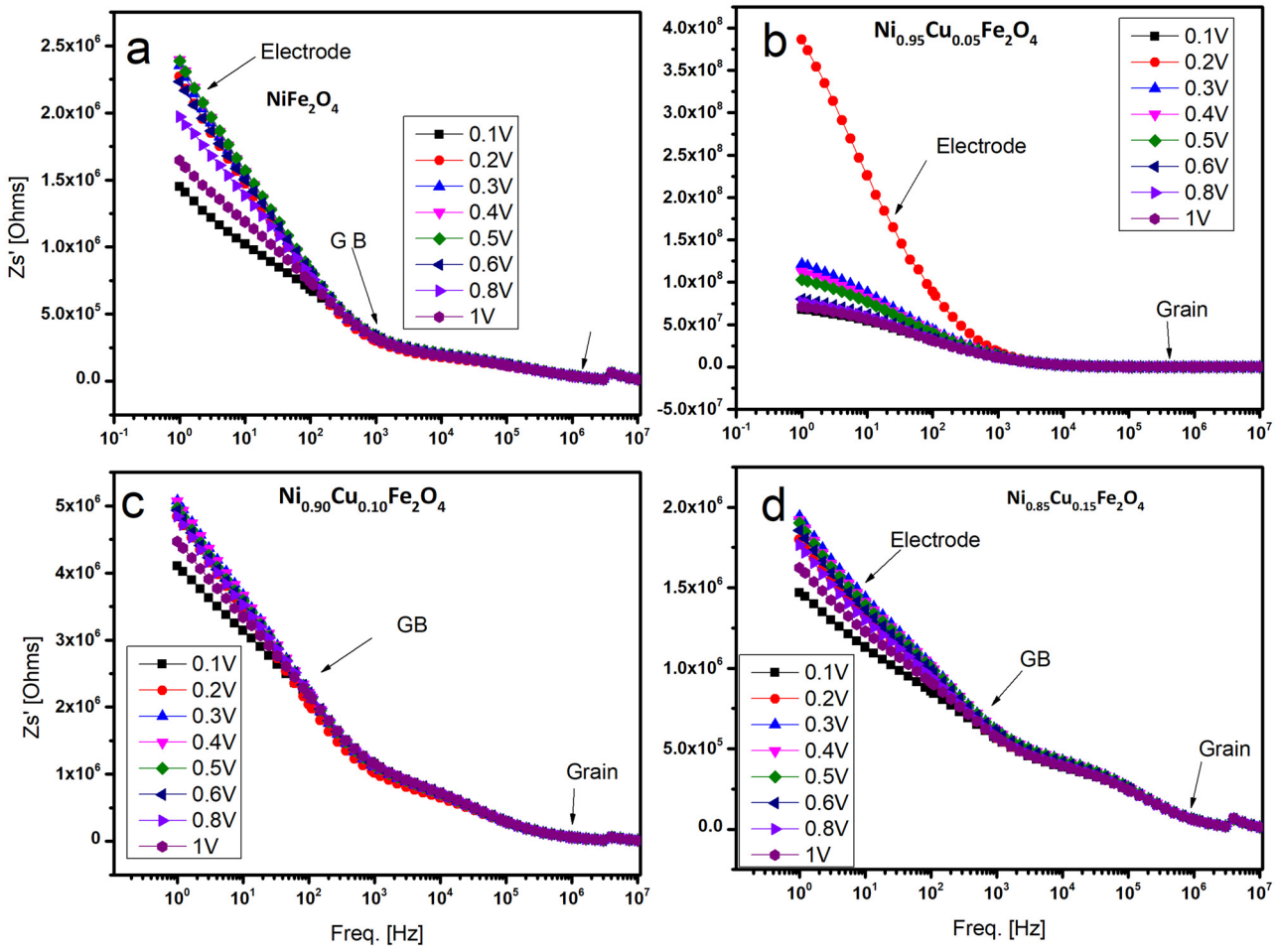

Figure 4: Variation of real impedance over frequency plots (a) $NiFe_2O_4$, (b) $Ni_{0.95}Cu_{0.05}Fe_2O_4$, (c) $Ni_{0.90}Cu_{0.10}Fe_2O_4$, and (d) $Ni_{0.85}Cu_{0.15}Fe_2O_4$ from 0.1 to 1 V.

(440), and (533) with maximum diffraction intensity from the (311) plane. The presence of all these planes confirms the existence of a cubic spinel structure which is consistent with the data file of JCPDS PDF card no. 003-0875. These results are also in agreement with the previous work of Sivakumar *et al.*, Maaz *et al.*, Shahane *et al.*, and Babu *et al.* [7,51–53]. Broad peaks were observed in the sample, demonstrating the lower degree of crystallization at a lower annealing temperature. These all values are in good agreement with the literature. The sharp diffraction peaks indicate a high degree of crystallization.

3.2 Scanning electron microscopy (SEM)

Morphological analysis of all synthesized samples was done using SEM. The JSM5910 model of Scanning Electron Microscope is used for imaging the prepared samples, which is manufactured by JEOL, Japan. It is installed in the centralized resource laboratory (CRL), University of Peshawar, Peshawar. The JSM5910 SEM images the samples at magnifications of 5,000 up to 60,000 at a voltage of 15 kV. SEM micrographs of the $NiFe_2O_4$ pellets at the magnifications of 10 and 5 µm for $Ni_{1-x}Cu_xFe_2O_4$ (where x = 0, 0.05, 0.10, 0.15,) sintered at 600°C are shown in Figure 2. It is visible from the micrographs that there are even-size grains both in the nano and bulk regimes. A number of interfaces are also seen in these micrographs. There might be a change in resistivity due to the decrease in the mean free path which occurs as a result of decreased grain size. From the micrographs, it is observed that there are well-connected grains and very little porosity is present in the samples; in addition, an increase in the copper content decreases the grain sizes slightly. The pore size as well as the number of pores in unit area slightly varies with area. It is also observed that some grains have sharp grain boundaries while few other grains are intermixed. Grains lie in the range of 1–5 µm size.

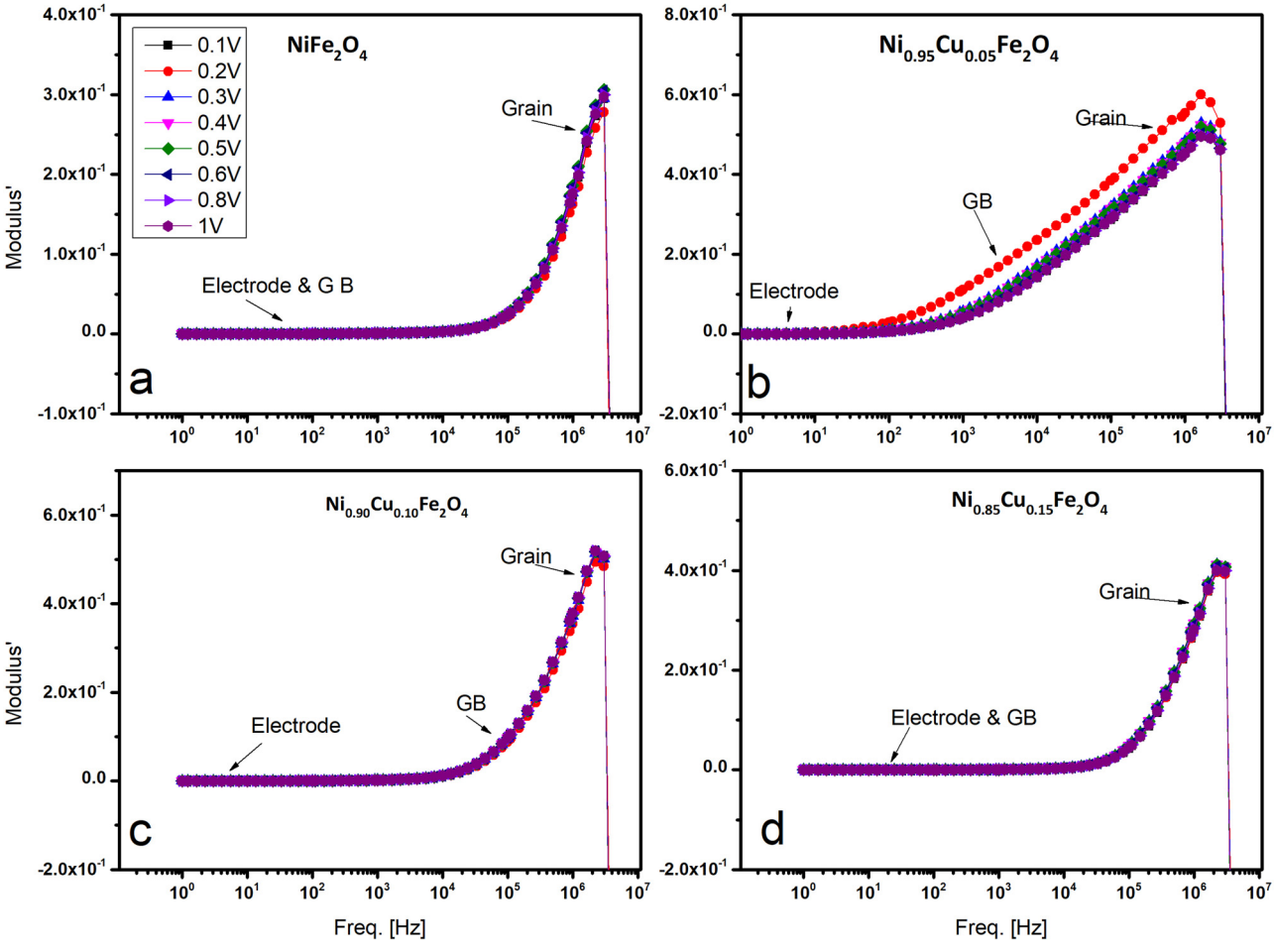

Figure 5: Frequency *vs* real part of modulus plots of (a) $NiFe_2O_4$, (b) $Ni_{0.95}Cu_{0.05}Fe_2O_4$, (c) $Ni_{0.90}Cu_{0.10}Fe_2O_4$, and (d) $Ni_{0.85}Cu_{0.15}Fe_2O_4$ from 0.1–1 V.

3.3 Impedance spectroscopy

Impedance spectroscopy is used for investigating the ac electrical properties of nickel ferrite $Ni_{1-x}Cu_xFe_2O_4$ (where x = 0, 0.05, 0.10, 0.15,...) and to analyze the existing electroactive regions. The effect of voltage on different parameters is observed over a wide frequency range. The results of Impedance spectroscopy of the $NiFe_2O_4$ system reveal the presence of grains, grain boundaries, and electrode semiconductor contacts which are the electroactive regions. Impedance data is taken in the frequency range of 1–3 × 10^7 Hz. Different AC signals from 0.1 to 1 V were applied for the collection of relevant impedance data. The temperature is kept at room temperature. In Figure 3(a)–(d), the complex impedance plots the lower values are due to the effect of grains, and then, the medium range of values occurred because of the grain boundaries while the presence of electrode effects yields the higher values in this plot.

Figure 4(a)–(d) shows the variation of real impedance over frequency. In these plots, the three electroactive regions are present at lower, intermediate, and higher values of frequencies. There are higher values of impedance at lower frequencies, the reason behind this is the effect of grains. In the medium frequency range, the impedance values are intermediate due to the effect of grain boundaries. At the end where the frequencies are lower the impedance values are greater owing to the considerable electrode effects.

In Figure 5(a)–(d), the effect of frequency on modulus' is demonstrated. In these plots at lesser frequencies, the values of real and imaginary parts of modulus are also lower, this phenomenon occurs because of the effects of electrode and grain boundaries; on the other side, the values are increasing considerably at the elevated frequencies, and this is due to the grain effect. Figure 6(a)–(d) show the plots between the real part of permittivity with frequency. At higher frequencies, the lower values of the

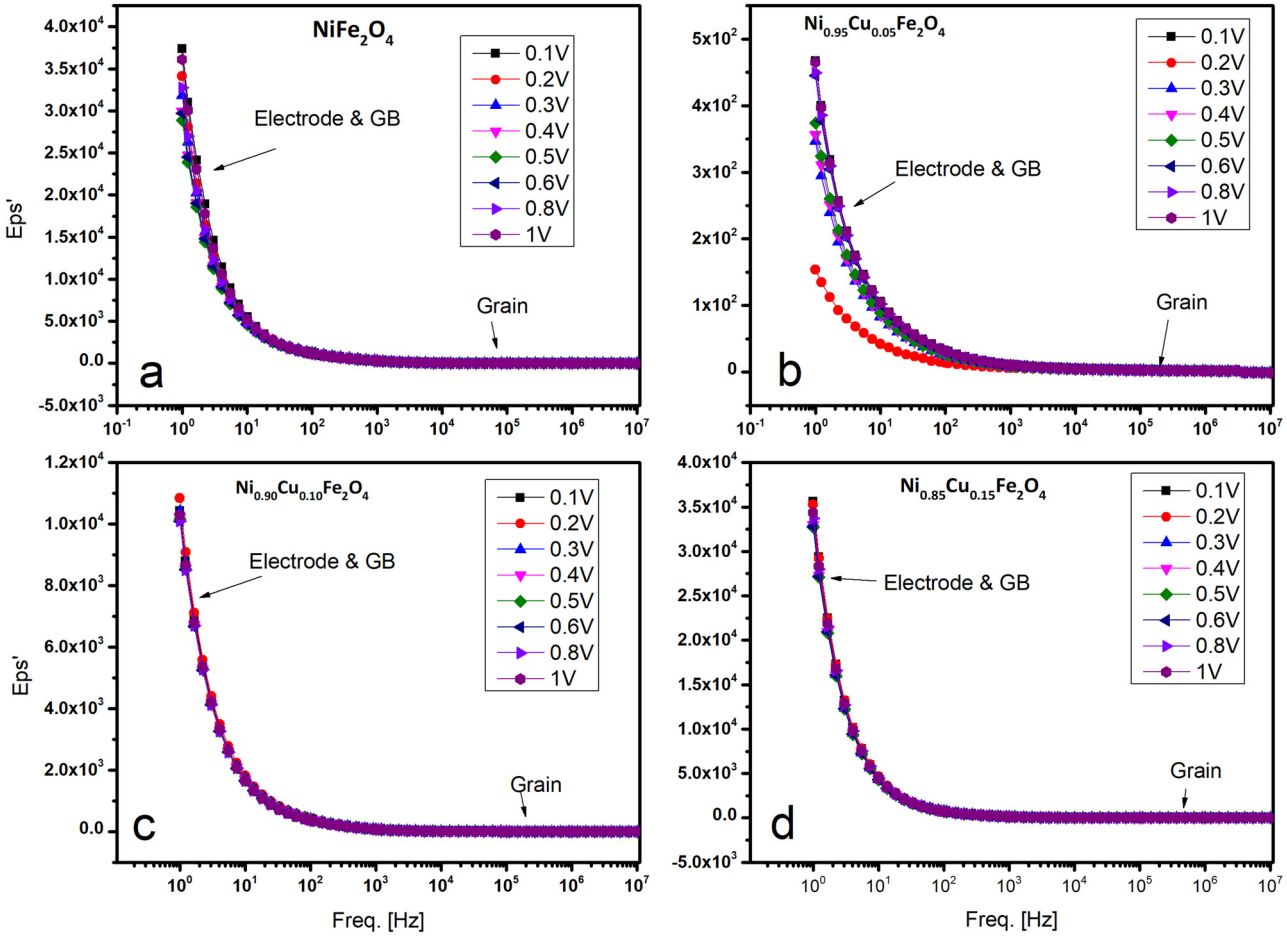

Figure 6: Variation of electrical permittivity' with frequency plots of (a) $NiFe_2O_4$, (b) $Ni_{0.95}Cu_{0.05}Fe_2O_4$, (c) $Ni_{0.90}Cu_{0.10}Fe_2O_4$, and (d) $Ni_{0.85}Cu_{0.15}Fe_2O_4$ from 0.1–1 V.

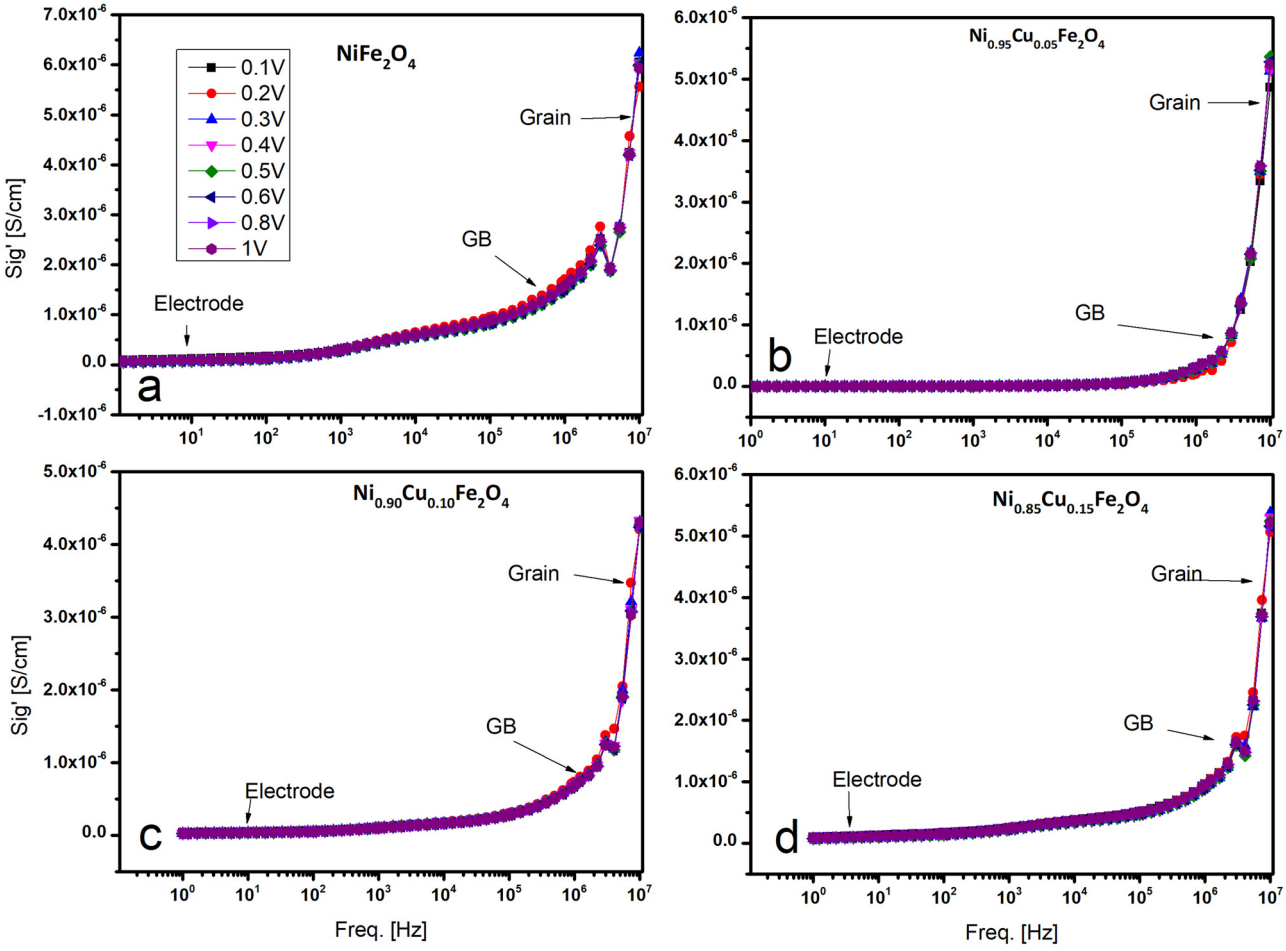

Figure 7: Frequency *vs* conductivity plots of (a) $NiFe_2O_4$, (b) $Ni_{0.95}Cu_{0.05}Fe_2O_4$, (c) $Ni_{0.90}Cu_{0.10}Fe_2O_4$, and (d) $Ni_{0.85}Cu_{0.15}Fe_2O_4$ from 0.1–1 V.

dielectric constant are due to grains while at lower frequencies the higher values of the dielectric constant correspond to interfacial effects, grain boundaries, and the electrode effect. The reduction in dielectric constant at elevated frequency values is quite a normal dielectric behavior [54,55]. The slight variations observed in the graphs for different compositions can be attributed to the saturation of the electroactive regions or the occurrence of the same electrical phenomenon in the voltage range.

In Figure 6(a)–(d), it is obvious that the dielectric permittivity is decreasing as the frequency is increased this phenomenon occurs because with the increase of copper concentration, there is a decrease in the concentration of nickel ions (Ni^{2+}). As a result of this, the Fe^{2+} ions yield less pairs for the hole, and ultimately, this results in electron hopping because of the buildup of charges across the grain boundaries which increase the resistance.

Figure 7(a)–(d) reveals the relation between frequency and ac conductivity. In 1977, Jonscher presented his famous power law [56–59]. The effect of frequency on the ac conductivity is elaborated in this law. A frequency-independent region represents the DC conductivity in the conductivity plot. It is then followed by an area where AC conductivity rises with the increase in frequency. The frequency from where the slope of the curve starts deviating is known as the hopping frequency. It is evident from the plot that the values of AC conductivity are lower at the lesser frequency end and they are higher at the larger frequency end the logic behind these variations is the electrode effect at the lower frequencies and the grain conductivity effect towards the higher frequency values. In between due to the grain boundaries effect, the values are intermediate at medium frequencies.

Figure 8(a)–(d) shows the dependence of tan delta with frequency. From this plot, three main regions can be noted prominently, where the values of tangent loss are lesser, medium, and higher. The reasons behind the noticeable variations in these values are the grains, grain boundaries, and electrode effects at the higher, medium, and lower frequency range, respectively. The frequency from where

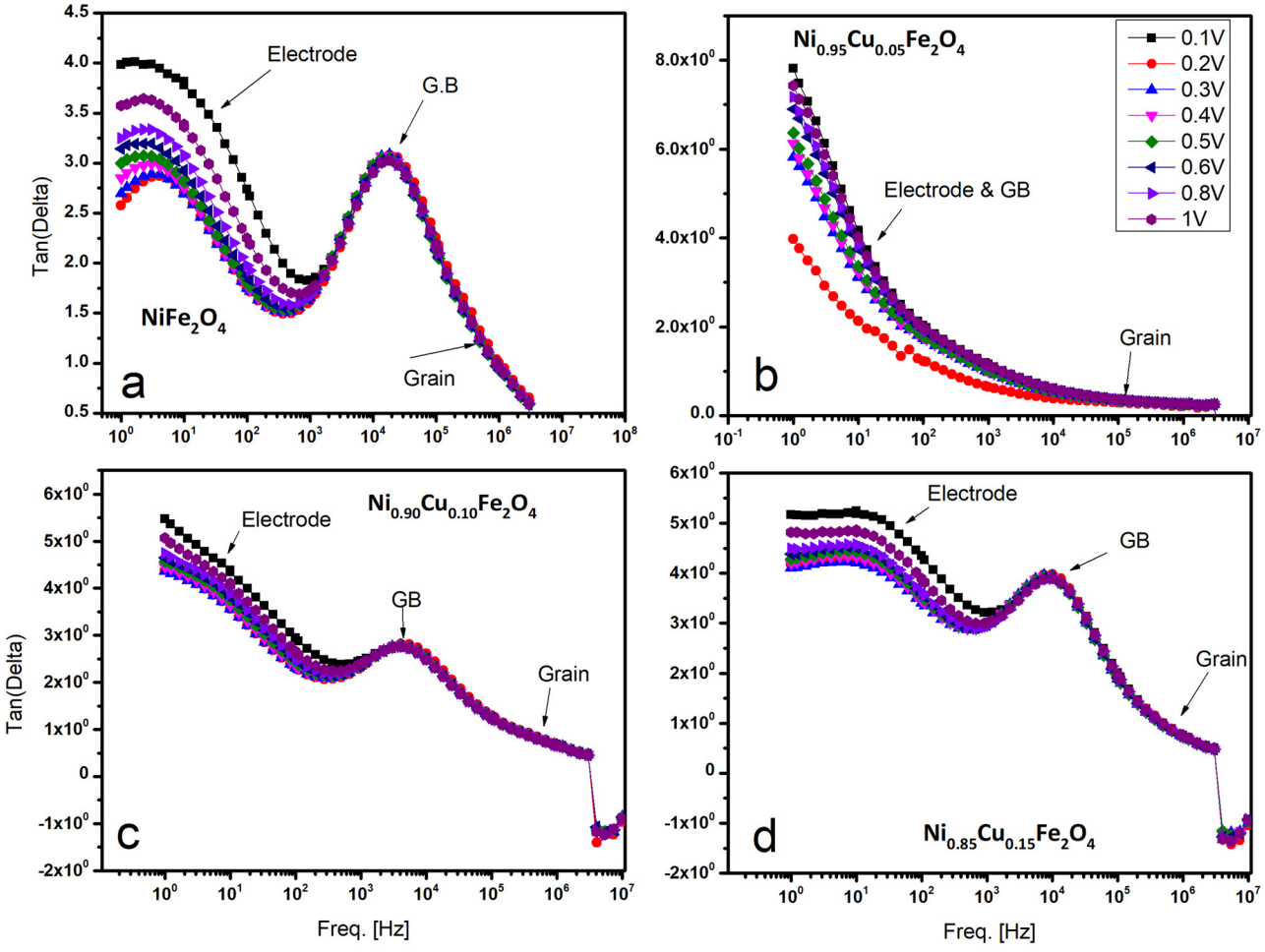

Figure 8: Frequency *vs* Tan Delta plots (a) $NiFe_2O_4$, (b) $Ni_{0.95}Cu_{0.05}Fe_2O_4$, (c) $Ni_{0.90}Cu_{0.10}Fe_2O_4$, and (d) $Ni_{0.85}Cu_{0.15}Fe_2O_4$ from 0.1–1 V.

the slope of the curve starts deviating is known as the hopping frequency.

4 Conclusions

Copper-doped $NiFe_2O_4$ particles with cubic spinal structure have been successfully synthesized by co-precipitation technique. XRD data confirmed the single-phase cubic spinel structure of copper-doped nickel ferrite nanoparticles. The lattice parameter has been calculated from the XRD pattern. The lattice parameter of Nickel ferrite was 8.34 Å and by increasing the copper concentration, the lattice parameter decreased by a small amount. The crystallite size of nickel ferrite calculated by Scherer's formula was about 40.83 nm which decreases with the increase in copper concentration. SEM analysis indicated that all the samples are nano-sized and homogeneous. SEM examination has shown that the grains are usually well connected and there is very little porosity. SEM indicated that with copper concentration increase, the grain sizes have decreased. Impedance spectroscopic results of $Ni_{1-x}Cu_xFe_2O_4$ (x = 0.05, 0.10, and 0.15) system show that there are three electroactive regions like G.B; grain and electrode are present. The conductivity decreases with increases in copper content. Modulus plots highlight the least capacitive phase of materials which are grains or bulk of materials whereas impedance plots highlight the more resistive phase of materials which are G.B and Electrodes or contacts. At higher frequencies, the lower value of permittivity is intrinsic whereas the higher value of permittivity at lower frequencies is extrinsic which is mainly due to interfacial effects.

Acknowledgments: SBK would like to acknowledge Dr. Javed Akhter and Dr. Mohammad Younas PINSTECH Islamabad for using their laboratory facilities for Impedance Spectroscopy. Thanks to Dr. Imran GC University of Faisalabad for helping me with pellet formation and XRD analysis of the samples. I would like to thank Dr. Manzoor Ahmad and Mr. Arshad for helping me with the SEM analysis. This work was

supported by Researchers Supporting Project number (RSP2024R243), King Saud University, Riyadh, Saudi Arabia.

Funding information: This work was funded by the Researchers Supporting Project Number (RSP2024R243) at King Saud University, Riyadh, Saudi Arabia. This work was supported by the National Research Foundation of Korea (NRF) grant funded by the Korea government (MSIT) (RS-2024-00357072).

Author contributions: Material preparation, data collection, and analysis were performed by Shabbir Ahmed Khan. The first draft of the manuscript was written by all authors and commented on previous versions of the manuscript. All authors have accepted responsibility for the entire content of this manuscript and approved its submission.

Conflict of interest: The authors state no conflict of interest.

Data availability statement: All data generated or analyzed during this study are included in this published article.

References

[1] Pullar RC. Hexagonal ferrites: A review of the synthesis, properties and applications of hexaferrite ceramics. Prog Mater Sci. 2012;57:1191–334.

[2] Guo J, Cai R, Cali E, Wilson GE, Kerherve G, Haigh SJ, et al. Low-temperature exsolution of Ni–Ru bimetallic nanoparticles from a-site deficient double perovskites. Small. 2022;18:1–10. doi: 10.1002/smll.202107020.

[3] Sagadevan S, Chowdhury ZZ, Rafique RF. Preparation and characterization of nickel ferrite nanoparticles *via* co-precipitation method. Mater Res. 2018;21:e20160533. doi: 10.1590/1980-5373-mr-2016-0533.

[4] Janudin N, Kasim NAM, Feizal Knight V, Norrrahim M, Razak M, Abdul Halim N, et al. Fabrication of a Nickel Ferrite/Nanocellulose-Based Nanocomposite as an Active Sensing Material for the Detection of Chlorine Gas. Polymers (Basel). 2022;14:1906. doi: 10.3390/polym14091906.

[5] Narang SB, Pubby K. Nickel Spinel Ferrites: A review. J Magn Magn Mater. 2021;519:167163. doi: 10.1016/j.jmmm.2020.167163.

[6] Zhao XG, Yang D, Ren JC, Sun Y, Xiao Z, Zhang L. Rational design of halide double perovskites for optoelectronic applications. Joule. 2018;2:1662–73. doi: 10.1016/j.joule.2018.06.017.

[7] Sivakumar P, Ramesh R, Ramanand A, Ponnusamy S, Muthamizhchelvan C. Preparation of sheet like polycrystalline NiFe2O4 nanostructure with PVA matrices and their properties. Mater Lett. 2011;65:1438–40.

[8] Raikher YL, Stepanov VI, Depeyrot J, Sousa MH, Tourinho FA, Hasmonay E, et al. Dynamic optical probing of the magnetic anisotropy of nickel-ferrite nanoparticles. J Appl Phys. 2004;96:5226–33.

[9] Cross WB, Affleck L, Kuznetsov MV, Parkin IP, Pankhurst QA. Self-propagating high-temperature synthesis of ferrites MFe2O4 (M = Mg, Ba, Co, Ni, Cu, Zn); reactions in an external magnetic field. J Mater Chem. 1999;9:2545–52.

[10] Song J, Chen Y, Hao X, Wang M, Ma Y, Xie J. Microstructure and mechanical properties of novel Ni–Cr–Co-based superalloy GTAW joints. J Mater Res Technol. 2024;29:2758–67.

[11] Yuhua C, Yuqing M, Weiwei L, Peng H. Investigation of welding crack in micro laser welded NiTiNb shape memory alloy and Ti6Al4V alloy dissimilar metals joints. Opt Laser Technol. 2017;91:197–202.

[12] Yang B, Wang H, Zhang M, Jia F, Liu Y, Lu Z. Mechanically strong, flexible, and flame-retardant Ti3C2Tx MXene-coated aramid paper with superior electromagnetic interference shielding and electrical heating performance. Chem Eng J. 2023;476:146834.

[13] Zhu Q, Chen J, Gou G, Chen H, Li P. Hydrogen embrittlement behavior of SUS301L-MT stainless steel laser-arc hybrid welded joint localized zones. J Mater Process Technol. 2017;246:267–75.

[14] Huang Z, Luo P, Wu Q, Zheng H. Constructing one-dimensional mesoporous carbon nanofibers loaded with NaTi2(PO4)3 nanodots as novel anodes for sodium energy storage. J Phys Chem Solids. 2022;161:110479.

[15] Luo P, Huang Z, Lyu Z, Ma X. In-situ fabrication of a novel CNTs-promoted Na3MnTi(PO4)3@C electrode in high-property sodium-ion storage. J Phys Chem Solids. 2024;188:111911.

[16] Zhao L, Fang H, Wang J, Nie F, Li R, Wang Y, et al. Ferroelectric artificial synapses for high-performance neuromorphic computing: Status, prospects, and challenges. Appl Phys Lett. 2024;124:30501.

[17] Guo J, He B, Han Y, Liu H, Han J, Ma X, et al. Resurrected and tunable conductivity and ferromagnetism in the secondary growth La0.7Ca0.3MnO3 on transferred SrTiO3 membranes. Nano Lett. 2024;24:1114–21.

[18] Zhao Y. Co-precipitated Ni/Mn shell coated nano Cu-rich core structure: A phase-field study. J Mater Res Technol. 2022;21:546–60.

[19] Patange SM, Shirsath SE, Jadhav SS, Lohar KS, Mane DR, Jadhav KM. Rietveld refinement and switching properties of Cr3 + substituted NiFe2O4 ferrites. Mater Lett. 2010;64:722–4.

[20] Kumar R, Kumar R, Kumar Sahoo P, Singh M, Soam A. Synthesis of nickel ferrite for supercapacitor application. Mater Today Proc. 2022;67:1001–4. doi: 10.1016/j.matpr.2022.05.433.

[21] Ishaq K, Saka AA, Kamardeen AO, Ahmed A, Alhassan MI, Abdullahi H. Characterization and antibacterial activity of nickel ferrite doped α-alumina nanoparticle. Eng Sci Technol an Int J. 2017;20:563–9. doi: 10.1016/j.jestch.2016.12.008.

[22] Rana G, Dhiman P, Kumar A, Vo DVN, Sharma G, Sharma S, et al. Recent advances on nickel nano-ferrite: A review on processing techniques, properties and diverse applications. Chem Eng Res Des. 2021;175:182–208. doi: 10.1016/j.cherd.2021.08.040.

[23] Ahmad U, Afzia M, Shah F, Ismail B, Rahim A, Khan RA. Improved magnetic and electrical properties of transition metal doped nickel spinel ferrite nanoparticles for prospective applications. Mater Sci Semicond Process. 2022;148:106830. doi: 10.1016/j.mssp.2022.106830.

[24] Chakradhary VK, Ansari A, Akhtar MJ. Design, synthesis, and testing of high coercivity cobalt doped nickel ferrite nanoparticles for magnetic applications. J Magn Magn Mater. 2019;469:674–80. doi: 10.1016/j.jmmm.2018.09.021.

[25] Chen L, Dai H, Shen Y, Bai J. Size-controlled synthesis and magnetic properties of NiFe2O4 hollow nanospheres *via* a gel-assistant hydrothermal route. J Alloy Compd. 2010;491:L33–8. doi: 10.1016/j.jallcom.2009.11.031.

[26] Bao N, Shen L, Wang Y, Padhan P, Gupta A. A facile thermolysis route to monodisperse ferrite nanocrystals. J Am Chem Soc. 2007;129:12374–5.

[27] Koli PB, Kapadnis KH, Deshpande UG. Nanocrystalline-modified nickel ferrite films: an effective sensor for industrial and

environmental gas pollutant detection. J Nanostruct Chem. 2019;9:95–110. doi: 10.1007/s40097-019-0300-2.
[28] Durgadsimi SU. Synthesis and structural analysis of nickel ferrite synthesized by co-precipitation method. Eurasian Phys Tech J. 2021;18:14–9. doi: 10.31489/2021No4/14-19.
[29] Kuang W, Wang H, Li X, Zhang J, Zhou Q, Zhao Y. Application of the thermodynamic extremal principle to diffusion-controlled phase transformations in Fe-C-X alloys: Modeling and applications. Acta Mater. 2018;159:16–30.
[30] Zhao Y, Sun Y, Hou H. Core-shell structure nanoprecipitates in Fe-xCu-3.0Mn-1.5Ni-1.5Al alloys: A phase field study. Prog Nat Sci Mater Int. 2022;32:358–68.
[31] Yang W, Jiang X, Tian X, Hou H, Zhao Y. Phase-field simulation of nano-α′ precipitates under irradiation and dislocations. J Mater Res Technol. 2023;22:1307–21.
[32] Zhang Y, He X, Cong X, Wang Q, Yi H, Li S, et al. Enhanced energy storage performance of polyethersulfone-based dielectric composite *via* regulating heat treatment and filling phase. J Alloy Compd. 2023;960:170539.
[33] Li H, Wu HZ, Xiao GX. Effects of synthetic conditions on particle size and magnetic properties of NiFe2O4. Powder Technol. 2010;198:157–66.
[34] Zhu S, Zhu J, Ye S, Yang K, Li M, Wang H, et al. High-entropy rare earth titanates with low thermal conductivity designed by lattice distortion. J Am Ceram Soc. 2023;106:6279–91.
[35] Jiang XJ, Bao SJ, Zhang LW, Zhang XY, Jiao LS, Qi HB, et al. Effect of Zr on microstructure and properties of TC4 alloy fabricated by laser additive manufacturing. J Mater Res Technol. 2023;24:8782–92.
[36] Zheng Z, Chen Y, Liu H, Lin H, Zhao H, Fang R, et al. Facile fabrication of NiFe2O4-FeNi/C heterointerface composites with balanced magnetic-dielectric loss for boosting electromagnetic wave absorption. Chem Eng J. 2024;481:148224.
[37] Long X, Chong K, Su Y, Du L, Zhang G. Connecting the macroscopic and mesoscopic properties of sintered silver nanoparticles by crystal plasticity finite element method. Eng Fract Mech. 2023;281:109137.
[38] Long X, Chong K, Su Y, Chang C, Zhao L. Meso-scale low-cycle fatigue damage of polycrystalline nickel-based alloy by crystal plasticity finite element method. Int J Fatigue. 2023;175:107778.
[39] Manohar A, Prabhakar Vattikuti SV, Manivasagan P, Jang ES, Bandi H, Al-Enizi AM, et al. Exploring NiFe2O4 nanoparticles: Electrochemical analysis and evaluation of cytotoxic effects on normal human dermal fibroblasts (HDF) and mouse melanoma (B16-F10) cell lines. Colloids Surf A Physicochem Eng Asp. 2024;682:132855.
[40] Gouadria S, Al-Sehemi AG, Manzoor S, Abdullah M, Ghafoor Abid A, Raza N, et al. Design and preparation of novel LaFeO3/NiFe2O4 nanohybrid for highly efficient photodegradation of methylene blue dye under visible light illumination. J Photochem Photobiol A Chem. 2024;448:115305.
[41] Singh A, Yadav K, Kumar R, Slimani Y, Sun AC, Thakur A, et al. ZnO-Cu/NiFe2O4 magnetic nanocomposite with boosted photocatalytic and antibacterial activity against E. coli. Nano-Struct Nano-Objects. 2024;37:101087.
[42] Gasser A, Ramadan W, Getahun Y, Garcia M, Karim M, El-Gendy AA. Feasibility of superparamagnetic NiFe2O4 and GO-NiFe2O4 nanoparticles for magnetic hyperthermia. Mater Sci Eng B. 2023;297:116721.
[43] Li W, Zhou X, Kang Y, Zou T, Li W, Ying Y, et al. Microstructure and magnetic properties of the FeSiAl soft magnetic composite with a NiFe2O4-doped phosphate insulation coating. J Alloy Compd. 2023;960:171010.
[44] Saha S, Routray KL, Hota P, Dash B, Yoshimura S, Ratha S, et al. Structural, magnetic and dielectric properties of green synthesized Ag doped NiFe2O4 spinel ferrite. J Mol Struct. 2024;1302:137409.
[45] Kumar A, Khanna K, Ram T, Dwivedi SK, Kumar S. Magnetic and magneto-dielectric properties of Nd3 + modified PbTiO3 and NiFe2O4 based multiferroic composites. Mater Today Proc. Epub ahead of print 2023. doi: 10.1016/j.matpr.2023.06.050.
[46] Sivaprakash P, Divya S, Esakki Muthu S, Ali A, Jaglicic Z, Hwan Oh T, et al. Effect of rare earth Europium (Eu3 +) on structural, morphological, magnetic and dielectric properties of NiFe2O4 nanoferrites. Mater Sci Eng B. 2024;301:117200.
[47] El Desouky FG, Saadeldin MM, Mahdy MA, El Zawawi IK. Tuning the structure, morphological variations, optical and magnetic properties of SnO2/NiFe2O4 nanocomposites for promising applications. Vacuum. 2021;185:110003.
[48] Patterson AL. The scherrer formula for X-ray particle size determination. Phys Rev. 1939;56:978–82. doi: 10.1103/PhysRev.56.978.
[49] Pubby K, Meena SS, Yusuf SM, Bindra Narang S. Cobalt substituted nickel ferrites *via* Pechini's sol–gel citrate route: X-band electromagnetic characterization. J Magn Magn Mater. 2018;466:430–45. doi: 10.1016/j.jmmm.2018.07.038.
[50] Belekar RM, Wani MA, Athawale SA, Kakde AS, Raghuvanshi MR. Minimum hysteresis loss and amplified magnetic properties of superparamagnetic Ni–Zn nano spinel ferrite. Phys Open. 2022;10:100099. doi: 10.1016/j.physo.2022.100099.
[51] Maaz K, Karim S, Mumtaz A, Hasanain SK, Liu J, Duan JL. Synthesis and magnetic characterization of nickel ferrite nanoparticles prepared by co-precipitation route. J Magn Magn Mater. 2009;321:1838–42 doi: 10.1016/j.jmmm.2008.11.098.
[52] Shahane GS, Kumar A, Arora M, Pant RP, Lal K. Synthesis and characterization of Ni-Zn ferrite nanoparticles. J Magn Magn Mater. 2010;322:1015–9. doi: 10.1016/j.jmmm.2009.12.006.
[53] Babu KV, Kumar GVS, Satyanarayana G, Sailaja B, Sailaja Lakshmi CC. Microstructural and magnetic properties of Ni1-xCuxFe2O4 (x = 0.05, 0.1 and 0.15) nano-crystalline ferrites. J Sci Adv Mater Devices. 2018;3:236–42. doi: 10.1016/j.jsamd.2018.04.003.
[54] Moradmard H, Farjami Shayesteh S, Tohidi P, Abbas Z, Khaleghi M. Structural, magnetic and dielectric properties of magnesium doped nickel ferrite nanoparticles. J Alloy Compd. 2015;650:116–22. doi: 10.1016/j.jallcom.2015.07.269.
[55] Ishaque M, Islam MU, Azhar Khan M, Rahman IZ, Genson A, Hampshire S. Structural, electrical and dielectric properties of yttrium substituted nickel ferrites. Phys B Condens Matter. 2010;405:1532–40. doi: 10.1016/j.physb.2009.12.035.
[56] Salim E, Tarabiah AE. The influence of NiO nanoparticles on structural, optical and dielectric properties of CMC/PVA/PEDOT:PSS nanocomposites. J Inorg Organomet Polym Mater. 2023;33:1638–45. doi: 10.1007/s10904-023-02591-2.
[57] Solanki PD, Oza MH, Jethwa HO, Joshi J, Joshi G, Jayavel R, et al. Nickel pyrophosphate nanoparticles: synthesis, structural, thermal, spectroscopic, and dielectric studies. Nano. 2022;17:2250049. doi: 10.1142/S1793292022500497.
[58] Bhuyan MDI, Das S, Basith MA. Sol-gel synthesized double perovskite Gd2FeCrO6 nanoparticles: Structural, magnetic and optical properties. J Alloy Compd. 2021;878:160389. doi: 10.1016/j.jallcom.2021.160389.
[59] Karmakar S, Behera D. High-temperature impedance and alternating current conduction mechanism of Ni0.5Zn0.5WO4 microcrystal for electrical energy storage application. J Aust Ceram Soc. 2020;56:1253–9. doi: 10.1007/s41779-020-00475-z.